Photoacoustics 33 (2023) 100546

Contents lists available at ScienceDirect

Photoacoustics

journal homepage: www.elsevier.com/locate/pacs

Ultrafast photoacoustic cavitation pumped by picosecond laser for high-efficient and long-term shockwave theranostics

Dandan Cui [a,b,1], Jie Mi [a,b,1], Zhenhui Zhang [a,b], Xiaoye Su [a,b], Xiaodong Sun [a,b], Gen Mu [a,b], Yujiao Shi [a,b,*], Sihua Yang [a,b,*]

[a] MOE Key Laboratory of Laser Life Science & Institute of Laser Life Science, College of Biophotonics, South China Normal University, Guangzhou 510631, China
[b] Guangdong Provincial Key Laboratory of Laser Life Science, College of Biophotonics, South China Normal University, Guangzhou 510631, China

ARTICLE INFO

Keywords:
Photoacoustic cavitation
Theranostics
Picosecond laser
Shockwaves

ABSTRACT

Photoacoustic (PA) theranostics is a new emerging field that uniquely combines diagnosis and treatment in one modality. However, its current status is compromised by the indispensable dependence on nonreversible phase-change nanoprobes that provides one-time-only action. Here, we demonstrate a picosecond-laser-pumped ultrafast PA cavitation technique for highly efficient shockwave theranostics, guaranteeing sustained PA cavitation by using non-phase-change nanoprobes. Theoretical simulations validate that, when compressing the excitation laser pulse width to hundred-picosecond, the thermal confinement effects of a conventional nanoprobe will induce transient heating of the extremely thin surrounding liquid layer of the nanoprobes beyond its cavitation point in a localized area at nanoscale, resulting in intense cavitation and PA shockwaves by the environment rather than the nanoprobes. Both cellular and mouse model experiments have demonstrated the highly effective anti-tumor effects. This method provides a sustainable, reproducible, and highly effective strategy for PA theranostics, prefiguring great potential for the clinical applications.

1. Introduction

For decades, breast cancer has become the most common cancer in women [1,2]. Developing reliable and effective cancer treatment methods is a primary concern in medical and clinical research. Currently, the clinical approaches of surgical resection, chemotherapy, and radiotherapy have certain limitations, such as irreparable tissue damage, drug resistance/radiation resistance [3–8], which fail to meet people's needs. Photothermal therapy (PTT) and photodynamic therapy (PDT) have recently gained widespread attention [9–12]. However, PTT still faces challenges due to the unpredictable and uneven distribution of the thermal field within the tumor, making it difficult to guarantee treatment effectiveness [11]. As for PDT, patients often experience varying degrees of photosensitivity reactions, severely affecting treatment outcomes [9]. Therefore, there is still an urgent need to develop new cancer treatment strategies that offer higher controllability, better efficacy, and greater safety.

Since discovered by A. G. Bell in 1880 [13], the photoacoustic (PA) effect has been wildly applied as an emerging technology in the fields of spectroscopy and biomedical imaging [14–20]. PA imaging uniquely combines the advantage of high-contrast of optical imaging with the depth-resolved capability of ultrasound imaging, providing outstanding opportunities for the noninvasive monitoring of disease pathophysiology in vivo [21–23]. Recently, by the aid of accurate organelle or subcellular organelle level localization with specific phase-change nanomaterials, a newly developed PA-cavitation-based disease treatment technique has been proposed for the rapid, selective and effective killing of diseased cells and tissues under the guidance of PA imaging [24–26]. In addition, using the cavitation mediated PA technique provides useful information for bubble mediated blood-brain barrier disruption or the increased cellular uptake of therapeutic drugs through cell membrane deformation [27], which allows non-invasive loading and unloading of macromolecules, and has far-reaching implications in diverse fields such as drug delivery and synthetic biology [28]. The generation, growth and subsequent collapse of the laser-triggered cavitation bubbles under the irradiation of pulsed laser will induce

* Corresponding authors at: MOE Key Laboratory of Laser Life Science & Institute of Laser Life Science, College of Biophotonics, South China Normal University, Guangzhou 510631, China.
E-mail addresses: shiyuj@scnu.edu.cn (Y. Shi), yangsh@scnu.edu.cn (S. Yang).
[1] These authors contribute equally to this work

https://doi.org/10.1016/j.pacs.2023.100546

Available online 23 August 2023

relative strong shockwaves [29], which can not only provide a more efficient PA energy conversion mechanism for imaging at relatively low laser power irradiation, but also introduce a nanoscale cavitation mediated PA therapy strategy by inducing transient mechanical forces that create irreversible localized damage to the diseased lesions [30]. Compared with conventional treatment methods, the PA therapy can effectively diminish the drug and radiation resistance with a well-defined therapy impact range, prefiguring a potential prospect with high treatment efficiency and good prognosis [24]. Meanwhile, the light dose used in PA imaging and therapy [31] is basically two or three orders of magnitude lower than that of photothermal (PT) therapy [32], which therefore can effectively avoid thermal damage to normal tissues. However, a commonly existed difficulty in current status is that efficient PA therapy indispensably depends on nonreversible cavitation nanomaterials such as phase-change-type nanoprobes with relatively low transition temperature or chemically-triggered gas-release-type nanomaterials [26], which usually provides one-time-only action with low stability and are impossible for long-term monitoring and treatment. Developing new shockwave excitation mechanism that breaks away from the dependence of specific nanoprobes in current PA imaging guided therapy by providing sustained PA cavitation output is an important step for further development and practical applications of PA shockwave theranostics.

Herein, the authors theoretically and experimentally proposed picosecond (ps)-laser-pumped PA cavitation technique as a new implementation of highly efficient and long-term shockwave theranostics, which can conquer the dependence of nonreversible cavitation nanomaterials and guarantee sustained PA cavitation output by directly using non-phase-change nanoprobes. Finite element analysis (FEA) simulation indicates that, when compressing the PA excitation pulse width from conventional tens of nanoseconds to hundreds of picoseconds with the same single pulse energy, the quick optical absorption and thermal confinement effects of the non-phase-change nanoprobes will induce transient heating of an extremely thin layer of surrounding liquid beyond its cavitation point. This induces the production of strong PA shock waves, thus realizing direct and sustainable PA cavitation by ultrafast superheating and fully getting rid of indispensably dependence of specific phase-change nanomaterials. PA experiments show that, cavitation phenomenon is observed under the ultrafast ps laser excitation, where the produced PA signal amplitude is several times higher than that of nanosecond (ns) laser with the same single pulse energy. Furthermore, both cellular and mouse model experiments have demonstrated the highly effective anti-tumor effects of this method. The proposed ultrafast PA cavitation is a technical innovation in PA theranostics and provides a new implementation of reproducible and highly efficient shockwave-mediated PA theranostics by getting rid of the unsustainable cavitation output limitation via phase-change-type nanoprobes, prefiguring great potential for the clinical applications of PA theranostics.

2. Materials and methods

2.1. Characterization of gold nanospheres (GNSs)

The structure of the GNSs was observed under a JEM-1400 PLUS transmission electron microscope (TEM) at 120 kV. The UV–vis absorption spectra were recorded on a spectrophotometer (Lambda-35 UV–vis spectrophotometer, PerkinElmer, MA, USA).

2.2. Experimental setup

Inject different concentrations of GNSs into the rubber tube, then fix and place it in the water tank. The sample is placed on a two-dimensional scanning stage, and the two-dimentional PA images are obtained by point-by-point scanning. The detected PA signal through a filter (BLP-21.4 +, Mini Circuits, New York, USA), and is amplified by an amplifier (LNA-650, RF Bay Inc, Maryland, USA), and finally collected by the digital acquisition card (M2p.5960, Germany). A computer was used for controlling the system and data processing. We used two high precision X-Y translation stage and their associated drives to gain precision of repetitive movement. The maximum amplitude projection was computed to construct an image.

2.3. Cell culture

EMT6 (Experimental Mammary Tumour-6) cells were cultured in DMEM with 10% FBS and 1% penicillin/streptomycin (PS) and maintained in a humidified cell culture incubator at 37 °C and with 5% CO_2.

2.4. Flow cytometry experiments

2.4.1. Flow compensation

About 2×10^6 cells were digested with digestion solution and suspended in 2 mL of culture medium, and evenly divided into 3 EP tubes. (1) Unstained group: Wash the cells once with PBS, collect by centrifugation (2500 rpm, 3 min), discard the supernatant, and add 500 μL binding buffer to suspend the cells (Fig. S5(a)). (2) AnnexinV-FITC staining group: cells were resuspended in 450 μL PBS and added with 50 μL H_2O_2, placed in an incubator for 20 min, centrifuged (2500 rpm, 3 min), washed once with PBS. Remove the supernatant and add 100 μL binding buffer to resuspend the cells. Add 5 μL of Annexin-V and mix well. Incubate at room temperature in the dark for 15 min, then add 400 μL binding buffer (Fig. S5(b)). (3) PI staining group: cells were resuspended in 500 μL PBS, placed in a constant temperature water bath at 70 °C for 20 min, collected by centrifugation (2500 rpm, 3 min), washed once with PBS, and the supernatant was removed. Add 100 μL binding buffer to suspend cells, add 5 μL of PI, mix well, incubate at room temperature in the dark for 15 min, and then add 400 μL binding buffer (Fig. S5(c)). Perform EMT6 compensation experiment gating settings as shown in the Supplementary Fig. S5. Determine the gate for FITC based on Fig. S5(b) and the gate for PI based on Fig. S5(c). Then, the control group gate was set and kept constant, applicable to all samples.

2.4.2. Experimental treatment

The EMT6 cells were cultured in 35 mm cell culture dishes at a density of approximately 1×10^6 cells/well. Then six groups of EMT6 cells treated with different conditions: (I) Control (PBS) group, (II) GNSs group, (III) 10 ns laser group, (IV) 350 ps laser group, (V) GNSs with 10 ns laser group, and (VI) GNSs with 350 ps laser group. For groups (II), (V) and (VI), GNSs were added to the 35 mm cell culture dish and co-incubated with the cells. For laser irradiation groups (III), (IV), (V) and (VI), we used a X-Y translation stage to control the scanning area, which was set at 2 cm × 2 cm. The concentration of the GNSs and the laser energy density for all groups are 200 μg/mL and 10 mJ/cm^2. After 12 h post-treatment, the cells were washed with PBS and collected by centrifugation (2500 rpm, 3 min). Suspend the cells with 100 μL binding buffer, and 5 μL AnnexinV-FITC and 5 μL PI were added and mixed. The mixture was incubated at room temperature in the dark for 15 min, followed by the addition of 400 μL binding buffer. Each sample was transferred to a flow cytometry tube using a pipette, gently mixed. Stained cells were measured on a flow cytometer (Beckman Coulter, CytoFLEX), with no antibodies used during the experiment. The dye molecules Annexin V-FITC and PI (Dojindo, AD10, Annexin V-FITC Apoptosis Detection Kit) used were used according to the protocol provided by the manufacturer. The flow cytometer was set to collect 10,000 cells in each group, with the collection channels automatically guided by the dye system used. All of the above steps were repeated three times in the experiment. Graphical analysis was performed using the CytExpert software package.

2.5. Confocal fluorescence imaging

Calcein-AM and PI solutions are used for staining live and dead cells, respectively (live cells in green and dead cells in red). The EMT6 tumor cells were inoculated into four confocal culture dishes (about 1×10^5 cells per well, 1 mL per well) and divided into four groups: (I) 10 ns laser, (II) 350 ps laser, (III) 10 ns laser+GNSs, and (IV) 350 ps laser+GNSs. For groups (III) and (IV), GNSs were added to the confocal culture dishes and co-cultured with cells for 12 h, with a GNSs concentration of 200 μg/mL in all groups. Then, 2 μL of Calcein-AM and 2 μL of PI were added together to 4 mL of fresh culture medium. After replacing the original culture medium with the fresh medium (1 mL per dish) in the four co-culture dishes, the cells were incubated in a cell culture incubator for 15 min. To demonstrate the precise cell killing induced by ps laser excitation and cavitation, the cell killing process was observed using a fluorescence confocal microscope (ZEISS, LSM880 With Airyscan). For excitation, the 488 nm line of an argon ion laser was attenuated with an acousto-optical tunable filter, reflected by a dichroic mirror (main beam splitter HFT 488), and focused through a Plan-Neofluar 40 /1.3 NA oil DIC objective (Carl Zeiss) onto the sample. Calcein-AM and PI emission were collected through 490–520 nm and 600–620 nm band pass filters, respectively. After completing the confocal image acquisition, the corresponding laser illumination treatment was performed, followed by continuing the observation of cell morphological changes under the confocal microscope. For laser irradiation, we used a X-Y translation stage to control the scanning area, which was set at 1 mm × 1 mm, and the laser energy density for all groups are 10 mJ/cm^2. Due to the movement of the confocal dishes before and after laser irradiation, markers were placed both on the confocal displacement stage and the confocal dishes to ensure accurate positioning of the imaging field before the illumination. Z-stacks were not used in the experiment. The analysis of the fluorescence images was performed using ZEN software, The images were directly exported and combined in Visio software. All of the above steps were repeated three times in the experiment.

2.6. In vivo PA therapy

Female Balb/c mice at 5–6 weeks of age were purchased from Southern Medical University (Guangzhou, China), and all animal experiments followed the Guide for the Care and Use of Laboratory Animals (Ministry of Science and Technology of China, 2006). The animal study protocol was approved by the Institutional Animal Care and Use Committee at South Normal University. A subcutaneous EMT6 tumor model was established by subcutaneously injecting the EMT6 cell suspension (density approximately 1×10^6) floating in 100 μL PBS into the back of 5–6 weeks old female Balb/c mice. When the tumor volume reached about 80 mm^3, EMT6 tumor-bearing female mice (5–6 weeks old) were prepared and randomly divided into two main groups, Group 1 and Group 2. The initial tumor volumes are the same for Group 1 and Group 2. Each main group was further divided into 6 subgroups (each consisting of 3 mice). (I) tail vein injection of PBS (control), (II) tail vein injection of GNSs, (III) 10 ns laser alone, (IV) 350 ps laser alone, (V) tail vein injection of GNSs with 10 ns laser, (VI) tail vein injection of GNSs with 350 ps laser. The GNSs concentration and laser energy density for all groups were 0.1 mg/mL (100 μL) and 10 mJ/cm^2, respectively. For laser irradiation groups (III), (IV), (V) and (VI), we used a X-Y translation stage to control the scanning area, which was set at 1 cm × 1 cm, covering almost the entire tumor region. The fast-axis speed of the system's motorized translation stage is set to 10 mm/s, and the slow-axis step is 20 μm, so the scanning time of the 1 cm × 1 cm imaging area was about 15 min. For Group 1, after the initial treatment on the first day, all mice received the same treatment every 4 days for a total of 20 days. During the treatment process, the relative tumor volume and mouse weight were monitored to evaluate the effective therapeutic effect of PA cavitation therapy on tumors and any potential side effects on the mice. All mice in the same group received the corresponding treatment. Tumor growth was measured by vernier caliper every 4 days for a total of 20 days and tumor volume was calculated by.

$$V = 0{\cdot}5 \times A \times B^2$$

where A refers to the tumor length and B refers to the tumor width. After completing the treatment, the survival rate curves of mice in different groups were monitored. When the tumor volume reaches approximately 1500 mm^3, we consider this as the endpoint for the mice. [33,34]. Relative tumor volume was defined as V per V_0 (V_0 is the tumor volume when the treatment was initiated) [33]. For Group 2, after the initial treatment on the first day, all mice received the same treatment every 4 days for a total of 20 days. On the 20th day, euthanasia is performed on all mice, and the tumor tissues of each group of mice were dissected and stained. The dissected tissues were fixed in 10% formalin, encapsulated in paraffin, sectioned, and stained with hematoxylin-eosin (H&E) and Ki67 antibody.

2.7. Statistical analysis

In this paper, data were statistically analyzed by Origin 2021 and Visio software. One-way analysis of variance (ANOVA) was used to compare whether there was a significant difference (p-value). All data are expressed as mean ± standard deviation (SD). The number of Ki67 positive cells and total cells were counted per field of view using Image-Pro Plus software.

3. Theory and results

Among the widely used nanomaterials for PA applications, the localized surface plasmon resonance (LSPR)-mediated metallic nanoparticles are one of the representative kinds benefiting from their good performance on optical absorption and bio-stability [35,36]. Here, we rationally choose the gold nanosphere (GNS) as the nanomaterial for demonstrating the ps laser pumped ultrafast PT and PA cavitation effect. When under light illumination, owing to the strong LSPR, free electrons in GNSs are quickly excited to high energy states above the Fermi level (within 50 femtoseconds) through electron–photon interactions [37]. The excited electrons then quickly release their kinetic energy non-radiatively to the lattice through electron–phonon interactions within picoseconds and induce temperature increase. When excited by conventionally used laser pulses with relatively long pulse width (usually 10 ns), owing to the small size effect of the nanoprobes, the laser pulse width is relatively large compared with the thermal confinement time, and the thermal confinement condition is no more applicable at the nanoscale [38]. Therefore, the GNS is slowly heated and suffers obvious thermal diffusion from the optically absorbing nanoparticle to its surrounding environment with a relatively long thermal length about 30 nm, as illustrated in the Fig. 1(a). Then, thermal expansion of both the heated GNS and its surrounding environment occurs and contributes to the production of the PA signal with relatively low conversion efficiency. Differently, when compressing the excitation pulse width to ps level by maintaining the single pulse energy unchanged, the quick heating of the GNS will easily induce transient temperature increase that beyond the cavitation point of the surroundings, which thus will induce phase transition of an extremely thin layer of surroundings from liquid to vapor, accompanied with intense PA cavitation and shockwave production through nanobubble expansion and collapse [39]. The ps laser pumped ultrafast PA cavitation provides a new strategy and controllable means for highly efficient PA theranostics by using non-phase-transition PA nanoprobes (indicated in Fig. 1(b)). The related physical process and their timescales are summarized in the Fig. 1(c).

To demonstrate the ultrafast PA cavitation and PT effect pumped by ps laser, quantitative study through FEA simulation is provided, with the comparison to ns pumped PA and PT effects. Refer to Table 1 for

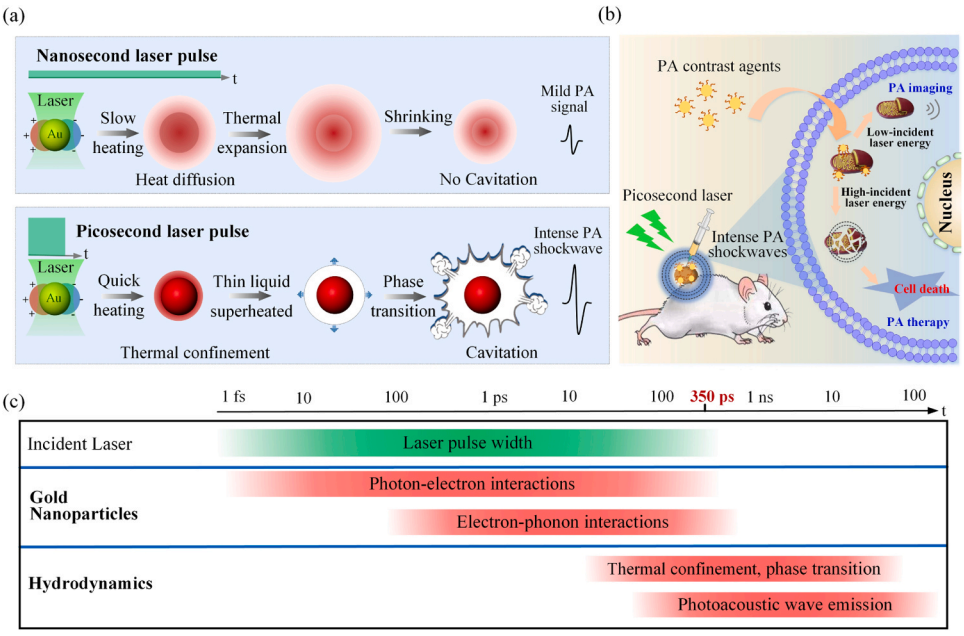

Fig. 1. Schematic illustration of the picosecond (ps) laser pumped ultrafast photoacoustic (PA) cavitation for high-efficient and long-term shockwave theranostics. (a) Comparison of the PA effect produced by conventionally used nanosecond (ns) laser pumped thermal expansion mechanism and the ps laser pumped PA cavitation mechanism. (b) The ps laser pumped ultrafast PA cavitation as new implementation of high-efficient and long-term shockwave theranostics. (**c**) The related physical process and their timescales of ps laser pumped ultrafast PA cavitation.

Table 1
Parameters used for air water and Au.

Symbol	Parameter	Values	Symbol	Parameter	Values
μ_0(Air)	relative permeability	1	ρ(H_2O)	density	1×10^3 kg/m^3
ε_0(Air)	the permittivity	1	σ(H_2O)	conductivity	5.5 μS/m
α(H_2O)	thermal diffusivity	1.4×10^{-3} cm^2/s	k(Au)	thermal conductivity	317 W/(m•k)
Δt_{th}	thermal confinement time	0.40 ns	α(Au)	thermal expansivity	14.2×10^{-6} 1/k
k(H_2O)	thermal conductivity	0.58 W/(m •k)	C_p (Au)	heat capacity	129 J/(kg•k)
α(H_2O)	thermal expansivity	70×10^{-6} 1/k	ρ(Au)	density	1.93×10^4 kg/m^3
C_p (H_2O)	heat capacity	4.2×10^3 J/(kg•k)	σ(Au)	conductivity	45.6×10^6 S/m

parameters used for air, water, and Au. When the GNS is irradiated by a time-harmonic electric field **E** with the frequency of ω and intensity of E0, the electric field distribution in and around the GNS can be described the Maxwell equations [40].

$$\nabla \times \mathbf{E} = -\frac{\partial \mathrm{B}}{\partial t} \tag{1}$$

$$\nabla \times \mathrm{B} = \mu_0 \mathrm{J} + \mu_0 \varepsilon_0 \frac{\partial \mathrm{E}}{\partial t} \tag{2}$$

Here μ_0, ε_0, J, **E** and **B** are the relative permeability, the permittivity, the current density, electric field intensity and magnetic induction intensity, respectively. When specifically targeted to the diseased area, the GNS can be reasonably considered as immersing in water environment. In our simulation, the diameter of the GNS is chosen to be 15 nm, and the electric field amplitude is set to be $1.15 \times 10^6 \mathrm{Vm}^{-1}$, which corresponds to a laser power density of 2.3 mW /μm^2. During the interaction of the GNS with incident laser, polarization and oscillations of the free electrons in the GNS occurs, which induces an enhanced electric field appears in the surface and a small area around the GNS. This phenomenon is known as the LSPR, and the electric field enhancement is presented in the Fig. 2(a). The activated free electrons in the GNS then release their kinetic energy to heat the GNS via electron-phonon interactions, where produced thermal energy (i.e. the absorbed optical energy) can be reasonably calculated as a resistive heating$Q_{abs} = \mathbf{J} \cdot \mathbf{E}$ in the FEA method, with **J** to be the current density due to free electron oscillations [41]. We quantitatively calculated the absorbed power of the GNS as a function of laser wavelength, as shown in the Fig. 2(b). The peek absorption wavelength that identified as the LSPR wavelength is at about 505 nm, with the peak absorbed laser power to be about 0.96 μW when under the laser irradiance of 2.3 mW/μm^2.

After the GNS releases its absorbed laser energy, the temperature of the GNS and its surroundings then increase, which can be described by the equation [42].

$$\rho C_p \frac{\partial T}{\partial t} = k \nabla^2 T + Q_{abs}(t) \tag{3}$$

with ρ, C_p, T and $k$to be the density, heat capacity, temperature and thermal conductivity, respectively. Q_{abs} is the thermal energy calculated as a resistive heating by the FEA simulation.

In conventional nanoprobe-assisted PA imaging and PA therapy, typically lasers with ns pulse width are used as the irradiation source. In these cases, owing to the small size-effect of the nanoprobes, the laser pulse width τ is relatively long compared with the nanoprobes' thermal confinement time [43].

$$\Delta t_{th} = D^2 / 4\alpha \tag{4}$$

Here, D is the diameter of the nanosphere, $\alpha$is the thermal diffusivity of the surroundings in the vicinity of the nanosphere, the thermal confinement time for the GNS is calculated to be 0.4 ns. Therefore, the thermal confinement condition is no longer applicable, and obvious thermal diffusion from the heated nanoprobes to surroundings can be observed during the laser pulse width, where the length of the heated surrounding layer is defined as $\chi = \sqrt{\alpha\tau}$ [43]. Here, we quantitatively simulated the temperature field distribution of a GNS and its surroundings irradiated by a pulsed laser with pulse width of 10 ns at the LSPR wavelength, with a certain single pulse energy of 9.6×10^{-9}μJ. As shown in the Fig. 2(c), during the laser pulse, the GNS is gradually

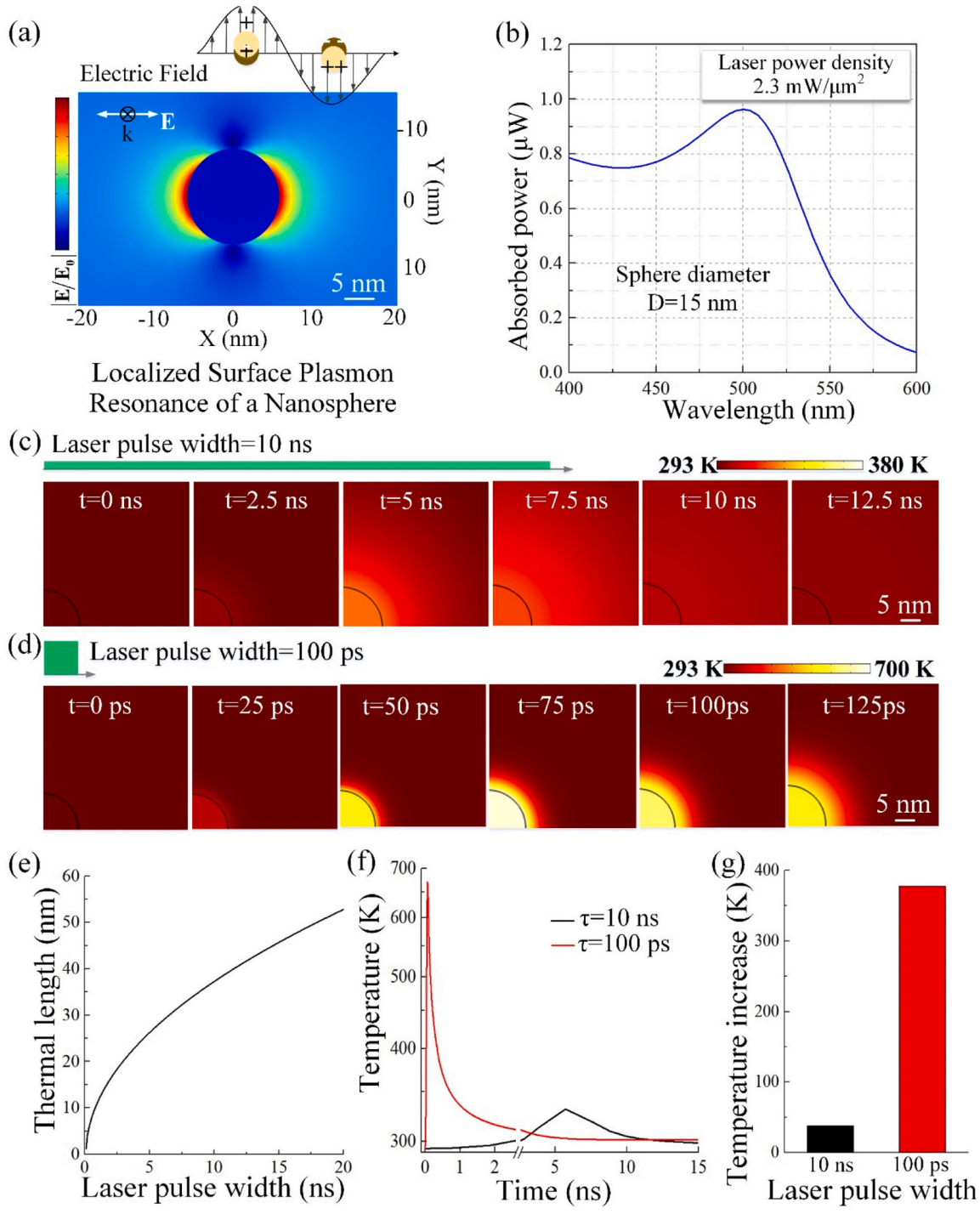

Fig. 2. Simulation results of optical and thermal responses of a gold nanosphere (GNS) pumped by ns and ps lasers with a certain single pulse energy of 9.6×10^{-9}μJ. (a) Electric field enhancement for a 15 nm water-immersed GNS. (b) The absorbed power as a function of wavelength for the GNS under 2.3 mW/μm^2 laser irradiation. (c) Time series of the temperature field for the GNS under 10 ns laser irradiation. (d) Time series of the temperature field for the GNS under 100 ps laser irradiation. (e) Thermal length in water as a function of the laser pulse width. (f) Temperature curves of the GNS with time under the irradiation of pulsed lasers with the same single pulse energy and different pulse widths. (g) Comparison of the temperature increase of the GNS for the two laser pulse widths.

heated up to higher temperature, accompanied by obvious thermal diffusion to its surroundings. When the laser pulse ends, the temperature of the GNS and its surrounding quickly decreases owing to thermal diffusion.

In ps laser pumped ultrafast PA applications, the nanoprobes are irradiated by a pulsed laser with much sharper laser pulse width that is relatively short compared with the thermal confinement time of the laser pulse width, and therefore the thermal confinement condition in this case can be well satisfied. Thus, when under the same single pulse energy irradiation, the nanoprobes are quickly heated up to a relatively higher temperature under the ultrafast irradiation, with negligible part of thermal energy diffused to surroundings. In Fig. 2(d), the authors quantitatively simulated the temperature field distribution of a GNS and its surroundings irradiated by a pulsed laser with pulse width of 100 ps, with the same single pulse energy of 9.6×10^{-9}μJ, by ignoring the potential phase transition of surroundings. It should be noticed that, owing

to the small-size-effect, the Laplace pressure [44] created by the liquid surface tension at the nanoprobe surface will result in the phase-transition temperature much higher than the macroscopic boiling temperature of water (373 K). Result shows that, during the laser pulse, the GNS is quickly heated up to a higher temperature that exceeds the cavitation point of surroundings (580 K) [45], with relatively small length of the heated surrounding layer, where the thermal length as a function of time is quantitatively simulated in the Fig. 2(e). The temperature waveforms with time of the GNS under the irradiation of pulsed lasers with the same single pulse energy and different pulse widths are quantitatively compared in the Fig. 2(f). Their temperature increase is quantitatively compared in Fig. 2(g). These results indicate that, even under the same single pulse energy irradiation, the temperature increase can reach up to nearly an order of magnitude higher in pico-second laser pumped ultrafast PA applications compared that of conventional PA imaging, predicting the great potential of the ultrafast PA applications in the field of high-efficient PA theranostics.

The temperature rises of the GNS and its surroundings will induce the production of PA waves with two mechanisms. In conventional PA imaging, usually a slow heating of the GNS and its surroundings occurs, and therefore the PA signal in this case is produced by thermal expansion of the heated area. In ultrafast PA applications, the transient temperature increase can exceed the cavitation point of the surroundings, and therefore produces strong phase transition and PA shock waves. The produced PA signal originates from thermal or nanobubble expansion induced displacement, by the equation [46].

$$\nabla P_{PA} = -\rho \frac{\partial^2 u}{\partial t^2} \tag{5}$$

where P_{PA} and u are the PA wave pressure and the radial displacement. Fig. 3(a) provides the produced quantitative displacement for the case of 10 ns laser pulse width. It shows that, the temperature rise introduces obvious thermal-expansion induced displacement of the GNS and its surrounding water layer, especially in the water layer owing to its relatively large thermal expansion coefficient, and contraction after the laser pulse ends. We quantified the PA pressure of the bubble-water boundary by tracking the thermal expansion induced total displacement according to Eq. (5), as shown in the Fig. 3(c), where the obtained in situ PA pressure is about 0.23 MPa.

As the model for GNS mediated cavitation is relatively complex to be analytically solved, the cavitation process and the nanobubble dynamics are performed by computational fluid dynamics (CFD) calculations with the GNS inside. For the case of ps laser pumped PA effect, owing to the supercritical heating of the GNS, intense nano-cavitation occurs and takes the role of PA shock wave production, where the nanobubble dynamics can be simulated by CFD method based on the Rayleigh-Plesset equation [47].

$$\rho\left(R\frac{d^2R}{dt^2}+\frac{3}{2}\left(\frac{dR}{dt}\right)^2\right) = P_{bubble} - P_0 - \frac{2\sigma}{R} - \frac{4\mu}{R}\frac{dR}{dt} \tag{6}$$

Here R is bubble radius, μ is viscosity and P_{bubble} is the pressure in the bubble. By assuming the bubble to be ideal gas, the bubble pressure is

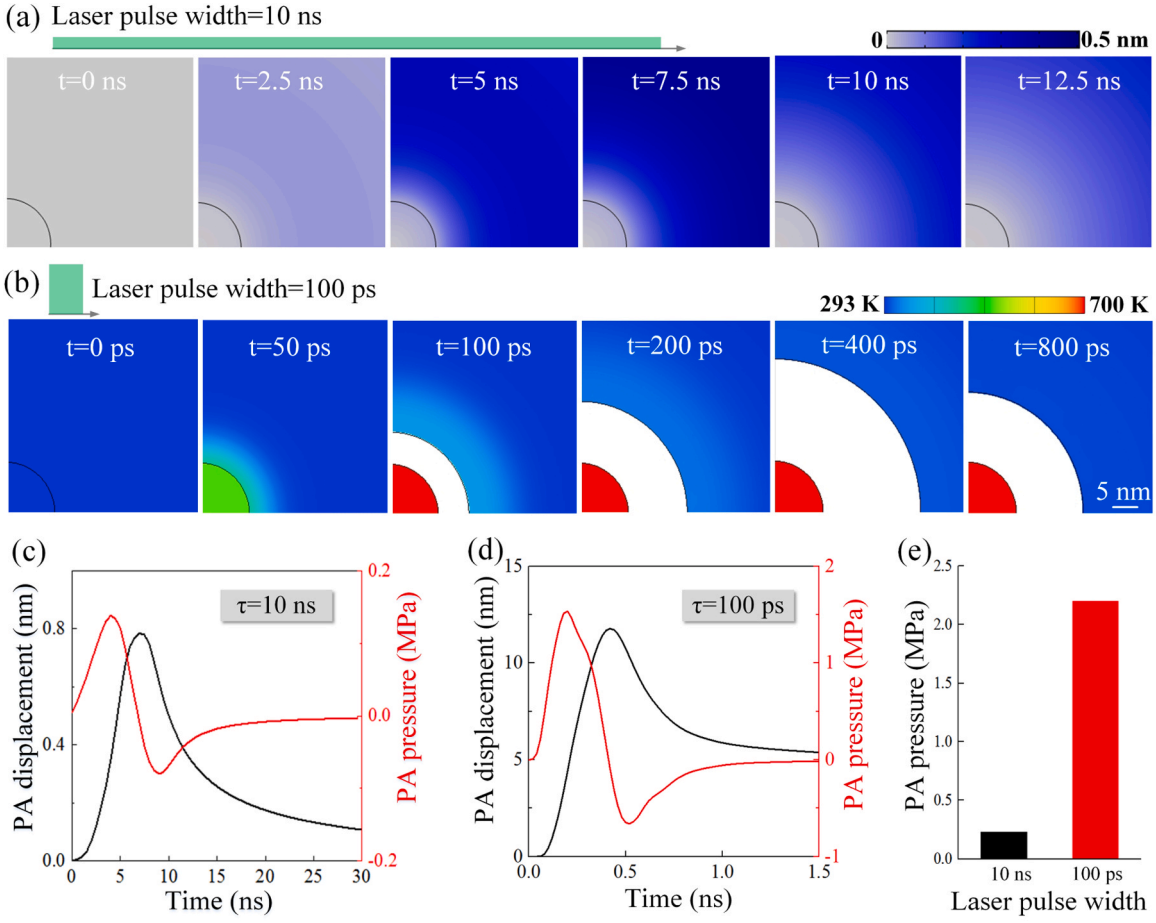

Fig. 3. Simulation results of PA response of the GNS pumped by ns and ps lasers with a certain single pulse energy of 9.6×10^{-9}μJ. (a) The thermal expansion induced PA displacement filed of the GNS under 10 ns laser irradiation. (b) The temperature fields and PA cavitation induced nanobubble formation of the GNS under 100 ps laser irradiation. (c) and (d) are the PA displacements and the corresponding PA pressures for the two pulse widths. (e) Quantitative comparison of the produced PA pressure by the two laser pulses with different pulse widths.

estimated according to the equation-of-state equation [45,48].

$$P_{bubble} = (\gamma - 1)\rho_{bubble} C_{bubble,V} T_{bubble} \quad (7)$$

where, $\gamma = C_{bubble,p}/C_{bubble,V}$, and $C_{bubble,p}$,$C_{bubble,V}$ are specific heat capacity at constant pressure and constant volume. The density, temperature and pressure are assumed to be homogeneous in the bubble, and the bubble density is dynamically evaluated as a function of time and temperature in the simulation. As the bubble expands, the bubble pressure and temperature decrease and the liquid pressure increases. When the pressure inside and outside the bubble equals, the bubble then suffers collapse. The simulated bubble formation and collapse process is indicated in the Fig. 3(b), and the corresponding PA displacement and PA signal induced by the bubble expansion and collapse is analyzed in the Fig. 3(d) according to the Eq. (5). Results indicate that, the ps laser pumped PA displacement can reach up to tens of nanometers, and the corresponding in situ PA pressure can reach up to about 2 MPa. The corresponding PA pressure for the two different pulse width with the same single pulse energy is quantitatively compared in the Fig. 3(e), showing that the ps laser pumped PA pressure is about one order of magnitude higher than that of the conventionally ns laser pumped PA pressure. These results provide theoretical foundations for the ps laser pumped ultrafast nano-cavitation medicated PA therapy.

To experimentally demonstrate the proposed idea, the ps laser pumped PA theranostics system is established, as shown in the Supplementary Fig. S1. A ps laser (MLC series Q-switched diode pumped solid state microchip lasers, France) with a pulse width of 350 ps, wavelength

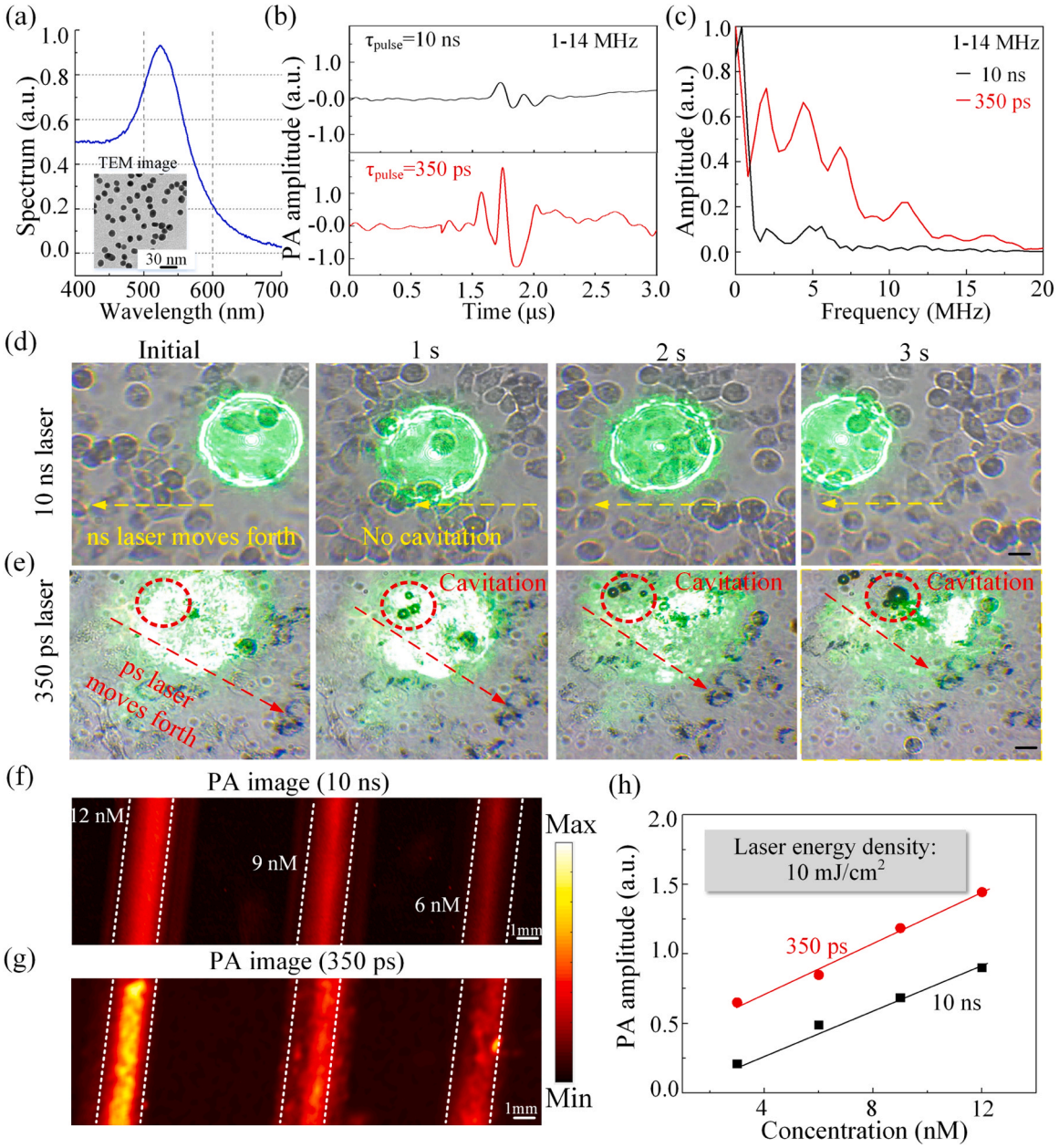

Fig. 4. Experimental results of the ps laser pumped PA cavitation for GNSs. (a) The optical absorption spectrum of the CNSs. The illustration shows the transmission electron microscopy (TEM) image of the GNSs. (b) PA signal of GNS under 10 ns and 350 ps pulsed laser irradiation using the hydrophone with a frequency band of 1–14 MHz. (c) The frequency spectra of PA signal of GNS under 10 ns and 350 ps pulsed laser excitation using the hydrophone with a frequency band of 1–14 MHz. (d) and (e) are the pictures of PA cavitation generated by EMT6 cells incubated with GNS for 6 h after ns laser or ps laser irradiation, scale bars are 20 μm. (f) and (g) are the PA images of GNSs with different concentrations under the irradiation of 10 ns and 350 ps pulsed lasers, respectively. The single pulse energy for the two lasers is controlled to be the same. (h) The PA signal amplitudes of the GNSs as a function of the concentration under the irradiation of 10 ns and 350 ps pulsed lasers.

of 532 nm, and repetition rate of 500 Hz is used as the pump laser source. Meanwhile, a ns laser (Model DTL-314QT, pulsed Q-switched lasers, Russia) with the same repetition and wavelength and a pulse width of 10 ns is used as the laser source for comparison study. During the experiments, the laser beams are expanded and spitted to two arms by a beam splitter. One arm is focused on the sample by an objective lens (NA=0.1), and the PA signals are received by the ultrasonic transducer and passed into the amplifier, and finally collected by the digital acquisition card. The other arm of laser is transferred to a power detector (S470c, United States) to measure the laser power. The sample is placed on an two-dimentional scanning stage. During the experiments, the laser fluence is controlled to below the American National Standards Institute safety limit [49].

Further, in order to verify the high energy conversion efficiency of the ps laser pumped PA system and its potentials for high-efficient PA therapy, related PA experiments on non-phase-change GNSs are performed. Fig. 4(a) is the optical absorption spectrum of the CNSs with an absorption peak of about 530 nm that well matched with the excitation laser wavelength. The GNS absorption peak is close to the simulated LSPR wavelength in Fig. 2(b). The illustration shows the TEM image of the GNSs, indicating an averaged diameter of about 15 nm. In order to quantitatively compare the PA conversion efficiency pumped by ps and ns lasers, GNSs with a concentration of 6 nM is prepared and tested. During the experiment, the energy density for the two lasers is controlled to be about 10 mJ/cm^2. The PA signals under the two lasers detected by the hydrophone with a frequency band of 1–14 MHz are shown in Fig. 4(b), and Fig. 4(c) are the spectrums of the GNSs PA signals, where the PA signal amplitude excited by ps laser is about two times larger than that of ns laser, indicating that the PA conversion efficiency excited by ps laser is higher than that by ns laser. The discrepancy between the experiments and simulations mainly arises from two aspects. Firstly, the frequency matching relation between the produced PA signal and the transducer is different when under the ps and ns laser excitation. As shown in the Supplementary Fig. S2, the theoretically calculated central frequencies of signals for the ps laser and ns laser are 750 MHz and 38 MHz, respectively. To experimentally demonstrate the frequency-dependent relationship between the PA signal and the pulse width of excitation laser, the authors performed a group of experiments obtained by all-optical PA remote sensing microscopy [50,51], the PA signal under 350 ps laser excitation is about one order of magnitude higher than that under 10 ns laser (Supplementary Fig. S3), which verifies our conjecture. High-frequency signals attenuate faster. However, the high-efficient and long-term shockwave thranostics proposed in our work depends on the in-situ PA shockwaves produced at the site of the nanoprobes to achieve mechanical damage at sub-micrometer scale, rather than the propagation of the PA waves far away. The authors simulated the attenuation of ultrasonic waves at different frequencies (750 MHz and 38 MHz) in water. As shown in Supplementary Fig. S4, Figs. S4(a) and S4(b) are the sound pressure nephograms of 750 MHz and 38 MHz ultrasonic waves propagating in water, respectively, showing that high-frequency signals attenuate faster. Figs. S4(c) and S4(d) are the corresponding sound pressure curves as a function of displacement. Supplementary Fig. S4(c) shows that the propagation distance for 750 MHz PA waves is about 0.6 μm when the attenuation reaches its half attenuation value, indicating that the high-frequency components can reasonably contributing to the high-efficient and long-term theranostics at sub-micrometer scale. Secondly, in simulation, the authors quantitatively compared the PA responses excited under laser pulse widths with three orders of magnitude difference (100 ps and 10 ns, respectively). While limited by the experimental condition, the pulse width of the ps laser used in experiments is 350 ps. The mis-match of the pulse width between the experiments and simulation could also contribute to the discrepancy.

To validate the ultrafast PA cavitation and PT effect pumped by ps laser, a high-resolution CCD is used to monitor the cavitation behavior of EMT6 cells incubated with GNS under the excitation of ps and ns lasers. It can be seen from Fig. 4(d) that no cavitation is observed as the position of the ns laser spot moves (see Video 1–2). Under ps laser irradiation, the recorded picture clearly shows cavitation as the ps laser spot moves toward the lower right corner. (Fig. 4(e)). From Video 4, it can be observed that after ps laser irradiation, there was a noticeable explosion phenomenon along with the formation of characteristic cavities in the targeted cell, especially near nanoparticle agglomerates. At the same time, the cell morphology changed obviously from a plump state to a fragmented state, indicating cell death [24,52] These results are the direct evidence for the ps laser pumped PA cavitation. Furthermore, three GNSs samples with different concentrations are injected into transparent tubes, and then imaged by the two lasers. The movement of the two lasers is controlled by X-Y translation stage, and their paths scan the sample along a bow. Fig. 4(f) and Fig. 4(g) are the obtained PA images under the 10 ns and 350 ps laser excitation, respectively. The sample shape is marked in the figure with a white dashed line. Results show that, the 350 ps laser pumped PA image exhibits much higher brightness compared with that of 10 ns laser, which coincides with the theoretical expectation and the experimental result in Fig. 4(b). Fig. 4(h) is the PA signal amplitudes as a function of the GNSs concentrations for the two lasers. These results validate the potential of ps laser pumped PA cavitation effect in high efficiency PA imaging and treatment.

Supplementary material related to this article can be found online at doi:10.1016/j.pacs.2023.100546.

Then, in order to demonstrate the ps laser pumped ultrafast PA nanocavitation mediated cytotoxicity, the Annexin V-FITC/PI staining assays are performed on EMT6 cells. As shown in the Supplementary Fig. S6, no obvious cell apoptosis is observed for the control, GNSs, 10 ns laser, 350 ps laser groups. While for the GNSs+ 10 ns laser and the GNSs+ 350 ps laser groups, cell death is observed, and there is a greater number of dead cells in GNSs+ 350 ps group. In order to further demonstrate the cavitation-induced precision cell killing when under ps laser excitation, the cell killing process observed by the fluorescence confocal microscopy is presented. The movements of the two lasers were controlled by a x-y stage motor, and their path ways were indicated by the white-dotted line. Further, corresponding confocal microscopy images of the survival conditions for the cells were recorded after different treatments. As shown in the Fig. 5(a), no obvious mortality of the cells was observed for the cells irradiated by ns laser. Encouragingly, large area effective killing of the cells was observed for the ps laser group. When cells were partially irradiated by ps laser, the distribution of cell death completely coincided with the scanning path of the laser. Furthermore, the explosion effect of ps-laser-excited cavitation on cells was verified by analyzing the local region in Fig. 5(a), as shown in Fig. 5 (b). After co-incubated with GNS, no matter irradiated by ns laser or not, the recorded images clearly showed that the cells had no obvious changes in morphology. However, after ps laser irradiation, the cell morphology clearly changed from a plump state to a fragmented one, and the bright red fluorescence confirmed the death of these cells, indicating the high efficiency of ps laser-induced PA cavitation therapy and heralding its great potential for clinical application.

To verify the effect of ps laser pumped PA treatment in vivo, EMT6 tumor-bearing female mice (5–6 weeks old) were prepared and randomly divided into two main groups, Group 1 and Group 2. The initial tumor volumes are the same for Group 1 and Group 2. Each main group was further divided into 6 subgroups (each consisting of 3 mice). (I) tail vein injection of PBS (control), (II) tail vein injection of GNSs, (III) 10 ns laser alone, (IV) 350 ps laser alone, (V) tail vein injection of GNSs with 10 ns laser, (VI) tail vein injection of GNSs with 350 ps laser. The schematic diagram of the treatment process is shown in Fig. 6(a). For Group 1, after the initial treatment on the first day, all mice received the same treatment every 4 days for a total of 20 days. During the treatment process, the relative tumor volume (Fig. 6(b)) and mouse weight (Fig. 6 (c)) were monitored to evaluate the effective therapeutic effect of PA cavitation therapy on tumors and any potential side effects on the mice. For the GNSs with 350 ps laser treated group, the tumor growth was

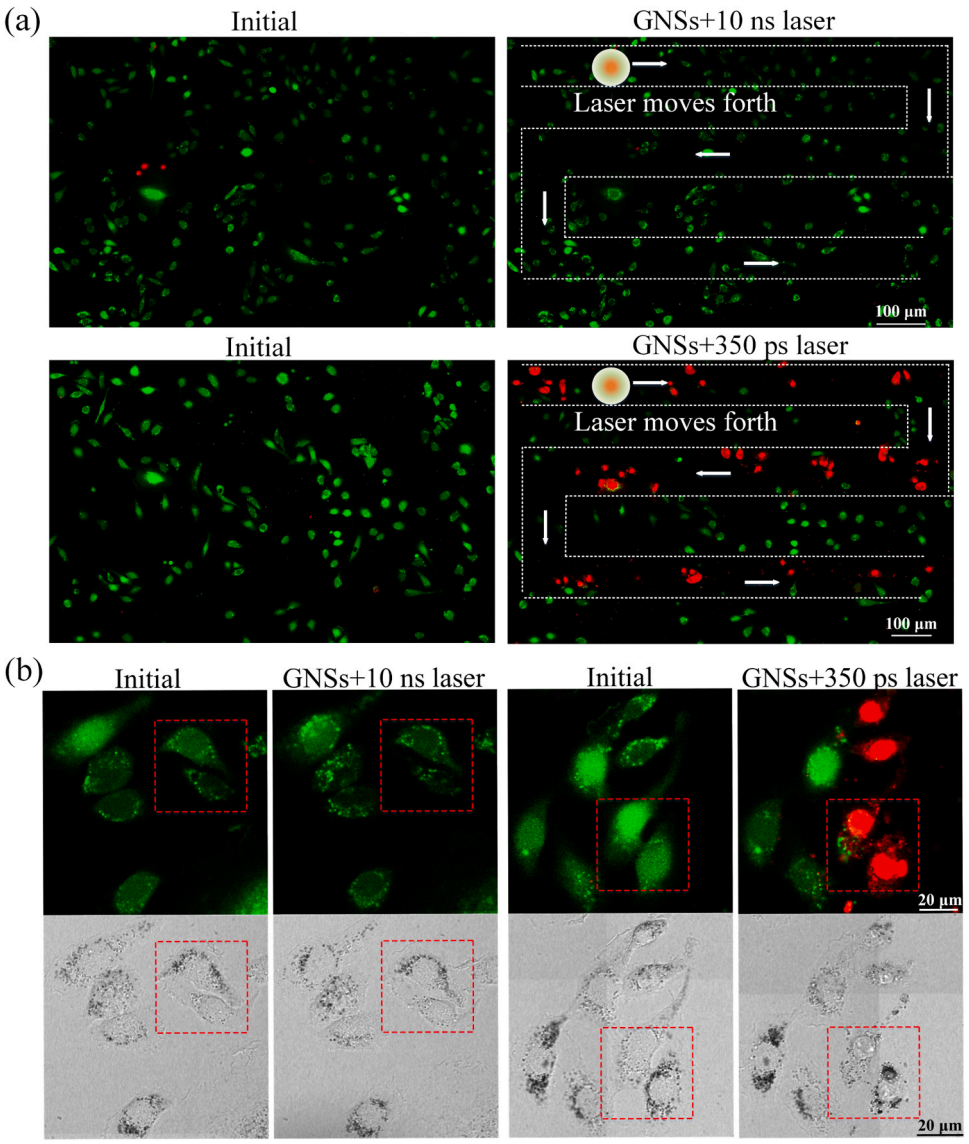

Fig. 5. PA cavitation induced cell killing effect on EMT6 cells. (a) Confocal laser scanning microscope (CLSM) images of calcein-AM and PI co-stained EMT6 cells after the various treatments. Calcein-AM staining (live cells) in green and PI staining (dead cells) in red. (b) The explosion effect of ps-laser-excited cavitation on cells was verified by confocal experiments.

suppressed, demonstrating that the effective therapeutic performance of ps laser-pumped PA therapy in vivo. The weight fluctuations of all mice were negligible, confirming that the side effects of these treatments on healthy mice could be ignored. The tumor inhibition rate of different groups was calculated by the formula: $(V_{Control} - V_{Experiment})/V_{Control}$ (Supplementary Fig. S7) [24]. We found a tumor inhibition rate of approximately 92.6 ± 1.5% after treatment with GNSs+ 350 ps, which had a significant tumor growth inhibitory effect. After completing the treatment, the survival rate curves of mice in different groups were monitored. When the tumor volume reaches approximately 1500 mm^3 , we consider this as the endpoint for the mice. It is worth noting that the average lifespan of mice in the other groups was 20–40 days. In contrast, tumors in the GNSs with 350 ps laser group were eradicated without further recurrence, and all treated mice survived for more than 50 days (Fig. 6(d)). For Group 2, after the initial treatment on the first day, all mice received the treatment every 4 days for a total of 20 days. On the 20th day, euthanasia is performed on all mice, and the tumor tissues of each group of mice were dissected and stained. The histological evaluation of tumor slices for the H&E staining showed, compared to other groups, the HE-stained sections of the GNSs+ 350 ps group exhibited severe nucleus shrinkage, plasmatorrhexis, and karyorrhexis, accompanied by obvious morphological changes, indicating a marked occurrence of tumor apoptosis, the Ki67 immunohistochemistry assays were also carried out to estimate the proliferative capacity of the tumors. As expected, Ki67 staining imaging showed that the proliferation of tumor cells was inhibited after GNSs+ 350 ps g treatment, which was consistent with the therapeutec outcome in Fig. 6(b) and Supplementary Fig. S7 showing that the tumor growth in the GNSs+ 350 ps treatment group was inhibited. The Ki67 positive rate was calculated using the formula: Ki67 positive rate = (Ki67 positive cell number / total cell number)× 100% [53]. The statistical results are shown in Supplementary Fig. S8. It can be seen that the Ki67 expression of the GNSs+ 350 ps group is lower than that of the other groups, only 10 ± 1.5%, indicating that the proliferation of tumor cells is significantly inhibited. To eliminate the impact of pulsed laser-induced thermal accumulation during the treatment process on the experiment, 980 nm continuous wave (CW) laser was utilized to irradiate gold nanorods, whereas 350 ps pulsed laser was utilized to irradiate GNSs. A comparison of the temperature rise curves of the two group reveal that the temperature increase generated by the ps laser irradiation of GNSs is nearly 1 ℃

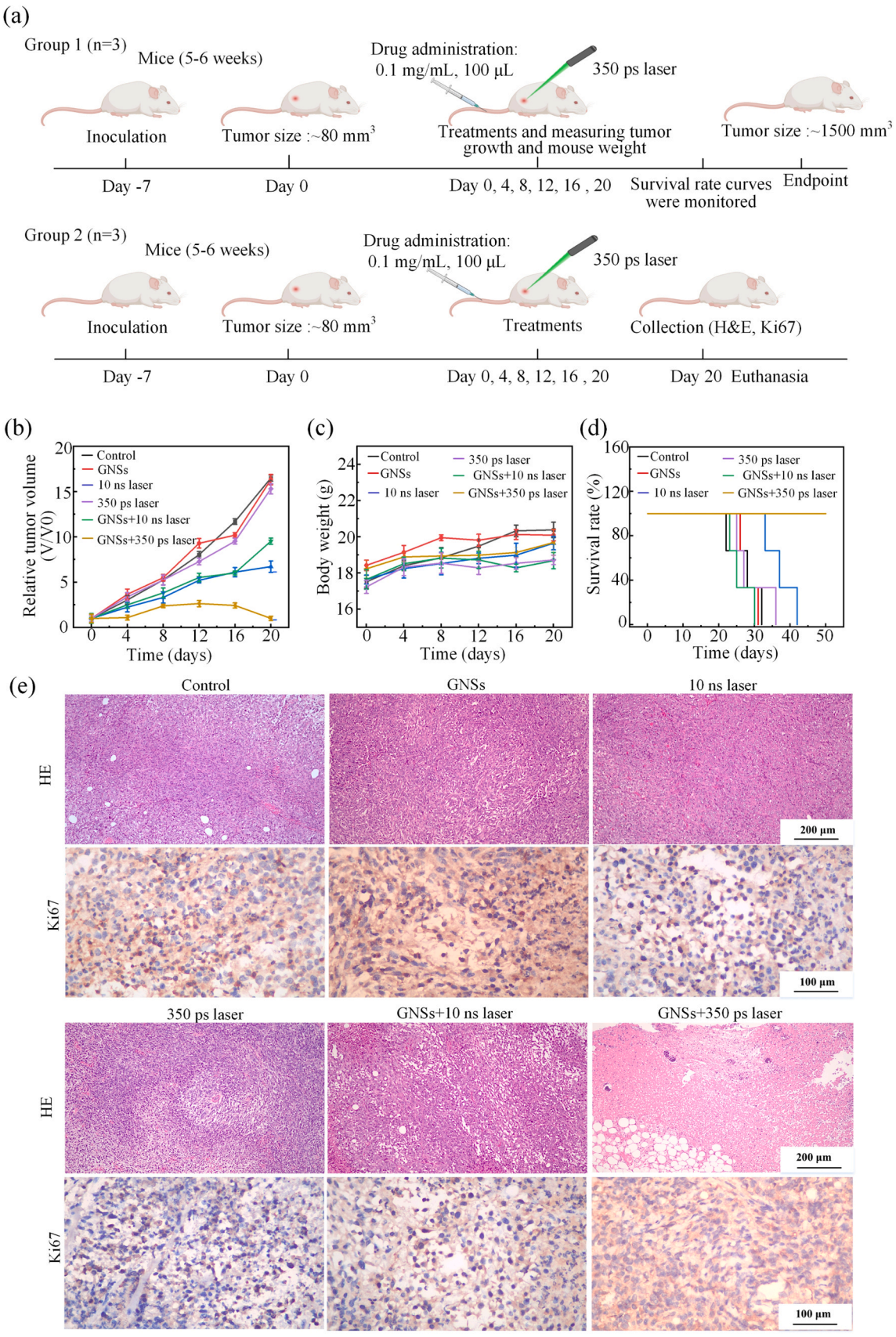

Fig. 6. In vivo antitumor effect. **(a)** Schematic diagram of the treatment process. **(b)** Relative tumor volume of each treatment group during treatment (n = 3). **(c)** Recorded the body weight changes of EMT6 tumor-bearing mice in different treatment groups during the treatment period. **(d)** Survival curves of EMT6 tumor-bearing mice under different treatment conditions. **(e)** Representative images of HE-stained and Ki67-stained slices of the tumor body after treatment.

(Supplementary Fig. S9), and the resulting thermal effect can be deemed negligible. As such, there is no risk of tissue damage due to thermal accumulation. In vivo antitumor experimental results showed that ps laser-pumped PA therapy had high efficiency under the same conditions as nanosecond laser therapy.

4. Discussion and conclusions

Compared to the existing PA cavitation therapy research that inevitably relies on the defect of irreversible cavitation nanomaterials, the proposed ultrafast PA cavitation by non-phase change nanoprobes eliminates the unsustainable cavitation output limitation, providing a new way to achieve reproducible and highly efficient shock wave mediated PA therapy diagnosis. In our work, comparison study on PT and PA effect is performed theoretically and experimentally for ps lasers and conventional ns lasers by controlling the single pulse energy to be a constant. The core point of the proposed method is the ps laser pumped ultrafast PA effect where the maximum temperature of the excited nanoprobes exceeds the cavitation point of surroundings, and therefore trigger the ultrafast PA cavitation effect. As indicated by the FEA simulation results in the Supplementary Fig. S10, there are two main aspect that contribute to the maximum temperature of the excited GNSs. By enhancing the power density of the ps laser, higher maximum temperature can be guaranteed, which however exists potential laser damage to biological tissue. Alternatively, higher maximum temperature can be obtained by further compressing the pulse width of the excitation laser with the single pulse energy to be a constant. Nevertheless, it should be noticed that, the overheating of the nanoprobes that exceeds their melting temperature (~1300 K) should be avoided in the experiments [54,55]. In addition, this work focuses on the theranostic mechanism of picosecond-laser-excited plasmonic-nanoparticle medicated nanocavitation, and a physically simple sphere model is chosen. Even though the peak absorption wavelength of the currently used GNS (532 nm) is not at the “tissue optical window”, the optical absorption wavelength can be easily tailored by controlling their morphologies. For example, by changing their shapes to nanorods, their peak optical absorption wavelength can be easily changed to the “tissue optical window” [56], thus benefiting their biomedical application in deep tissues.

In conclusion, an ultrafast PA cavitation technique pumped by ps laser is proposed as a new implementation of high-efficient and long-term shockwave theranostics. FEA simulations proved that, the quick optical absorption and thermal confinement effects of a conventional nanoprobe under the excitation of ps laser can induce transient heating of a thin surrounding liquid layer beyond its cavitation point, thus producing intense cavitation and PA shockwaves. In vitro cell experiments observed the phenomenon of ultrafast cavitation, with precise cavitation and explosion occurring at the GNSs sites. In vitro phantom experiments confirmed that the amplitude of the PA signal was several times higher than that of ns laser. Both cellular level and mouse model experiments have demonstrated the high-precision and good-efficacy of the proposed anti-tumor method. This work technically promotes advances the traditional implementation of the PA image-guided therapy by ps laser pumped sustainable ultrafast cavitation of non-phase-change nanoprobes, prefiguring great potential for the clinical applications of high-efficient and long-term shockwave theranostics.

CRediT authorship contribution statement

D. D. Cui, J. Mi, Z. H. Zhang, X. Y. Su, X. D. Sun., G. Mu, Y. J. Shi. and S. H. Yang designed the experiment. D. D. Cui, J. Mi, Z. H. Zhang, and G. Mu, contributed to the system construction and performed the sample fabrications. D. D. Cui, J. Mi, X. Y. Su, and X. D. Sun, performed the experiment and data analysis. D. D. Cui and J. Mi wrote the draft of the manuscript. Y. J. Shi. and S. H. Yang supervised the project. D. D. Cui, J. Mi, Z. H. Zhang, X. Y. Su, X. D. Sun, G. Mu, Y. J. Shi. and S. H. Yang were involved in discussions. All authors took part in the discussion and revision and approved the final copy of the manuscript.

Declaration of Competing Interest

The authors declare that they have no known competing financial interests or personal relationships that could have appeared to influence the work reported in this paper.

Data Availability

Data will be made available on request.

Acknowledgements

National Natural Science Foundation of China (Nos. 62335007, 61627827, 61805085), Science and Technology Planning Project of Guangdong Province, China (Nos. 2015B020233016, and 2018A030310519), the Guangzhou Science and Technology Plan project (No. 201904010321), the Science and Technology Program of Guangzhou (No. 2019050001).

Appendix A. Supporting information

Supplementary data associated with this article can be found in the online version at doi:10.1016/j.pacs.2023.100546.

References

[1] A.N. Giaquinto, H. Sung, K.D. Miller, J.L. Kramer, L.A. Newman, A. Minihan, R. L. Siegel, Breast cancer statistics, 2022, CA: a Cancer J. Clin. 72 (6) (2022) 524–541.
[2] M. Arnold, E. Morgan, H. Rumgay, A. Mafra, D. Singh, M. Laversanne, I. Soerjomataram, Current and future burden of breast cancer: Global statistics for 2020 and 2040, Breast 66 (2022) 15–23.
[3] N.R. Patel, B.S. Pattni, A.H. Abouzeid, V.P. Torchilin, Nanopreparations to overcome multidrug resistance in cancer, Adv. Drug Deliv. Rev. 65 (2013) 1748–1762.
[4] R.K. Yuan, Y. Hou, W. Sun, J. Yu, X. Liu, Y.N. Niu, J.J. Lu, X.P. Chen, Natural products to prevent drug resistance in cancer chemotherapy: a review, Ann. Ny. Acad. Sci. 1401 (2017) 19–27.
[5] D.J. Fu, D.C. Liu, L.B. Zhang, L.M. Sun, Self-assembled fluorescent tripeptide nanoparticles for bioimaging and drug delivery applications, Chin. Chem. Lett. 31 (2020) 3195–3199.
[6] Q.Q. Hu, L. Bai, Z.J. Zhu, Z.G. Sun, P. Bai, M.H. Tang, C.X. Dou, J.F. Yan, R.S. Tong, W.Y. Zhang, L.J. Chen, β-Elemene-loaded polymeric micelles intensify anti-carcinoma efficacy and alleviate side effects, Chinese, Chem. Lett. 31 (2020) 915–918.
[7] G.S. Song, L. Cheng, Y. Chao, K. Yang, Z. Liu, Emerging nanotechnology and advanced materials for cancer radiation therapy, Adv. Mater. 29 (2017) 1700996.
[8] G. He, X. Yan, Z.H. Miao, H.S. Qian, Y. Ma, Y. Xu, L. Gao, Y. Lu, Z.B. Zha, Anti-inflammatory catecholic chitosan hydrogel for rapid surgical trauma healing and subsequent prevention of tumor recurrence, Chinese, Chem. Lett. 31 (2020) 1807–1811.
[9] Y.C. Song, L. Wang, Z.G. Xie, Metal–organic frameworks for photodynamic therapy: emerging synergistic cancer therapy, Biotechnol. J. 16 (2021) 1900382.
[10] Y. Li, X. Liu, W. Pan, N. Li, B. Tang, Photothermal therapy-induced immunogenic cell death based on natural melanin nanoparticles against breast cancer, Chem. Commun. 56 (9) (2020) 1389–1392.
[11] J.R. Peng, Y. Xiao, W.T. Li, Q. Yang, L.W. Tan, Y.P. Jia, Y. Qu, Z.Y. Qian, Photosensitizer micelles together with IDO inhibitor enhance cancer photothermal therapy and immunotherapy, Adv. Sci. 5 (2018) 1700891.
[12] Y. Yang, W.J. Zhu, Z.L. Dong, Y. Chao, L. Xu, M.W. Chen, Z. Liu, 1D coordination polymer nanofibers for low-temperature photothermal therapy, Adv. Mater. 29 (2017) 1703588.
[13] A.G. Bell, On the production and reproduction of sound by light, Am. J. Sci. 20 (1880) 305.
[14] J. Kim, G. Kim, L. Li, P. Zhang, J.Y. Kim, Y. Kim, H.H. Kim, L.V. Wang, C. Kim, Deep learning acceleration of multiscale superresolution localization photoacoustic imaging, Light-Sci. Appl. 11 (1) (2022) 1–12.
[15] J. Zhang, D. Peng, W. Qin, W. Qi, X. Liu, Y. Luo, L. Xi, Organ-PAM: Photoacoustic Microscopy of Whole-organ Multiset Vessel Systems, Laser Photonics Rev. (2023) 2201031.
[16] L. Lin, X. Tong, S. Cavallero, Y. Zhang, S. Na, R. Cao, L.V. Wang, Non-invasive photoacoustic computed tomography of rat heart anatomy and function, Light-Sci. Appl. 12 (1) (2023) 12.
[17] L. Lin, L.V. Wang, The emerging role of photoacoustic imaging in clinical oncology, Nat. Rev. Clin. Oncol. 19 (6) (2022) 365–384.

[18] Y. Liu, X. Yang, D. Zhu, R. Shi, Q.M. Luo, Optical clearing agents improve photoacoustic imaging in the optical diffusive regime, Opt. Lett. 38 (20) (2013) 4236–4239.
[19] Z. Gao, Y. Shen, D. Jiang, Y. Zheng, F. Liu, F. Gao, Implementation and comparison of three image reconstruction algorithms in FPGA towards palm-size photoacoustic tomography, IEEE Sens. J. (2023).
[20] A.A. Oraevsky, S.L. Jacques, F.K. Tittel, Measurement of tissue optical properties by time-resolved detection of laser-induced transient stress, Appl. Opt. 36 (1) (1997) 402–415.
[21] L.M. Nie, S.J. Wang, X.Y. Wang, P.F. Rong, Y. Ma, G. Liu, P. Huang, G.M. Lu, X. Y. Chen, In vivo volumetric photoacoustic molecular angiography and therapeutic monitoring with targeted plasmonic nanostars, small 10 (8) (2014) 1585–1593.
[22] X. Zhu, Q. Huang, A. DiSpirito, T. Vu, Q. Rong, X. Peng, H. Sheng, Q. Zhou, L. Jiang, U. Hoffmann, J. Yao, Real-time whole-brain imaging of hemodynamics and oxygenation at micro-vessel resolution with ultrafast wide-field photoacoustic microscopy, Light-Sci. Appl. 11 (1) (2022) 1–15.
[23] A.B.E. Attia, G. Balasundaram, M. Moothanchery, U.S. Dinish, R. Bi, V. Ntziachristos, M. Olivo, A review of clinical photoacoustic imaging: Current and future trends, Photoacoustics 16 (2019), 100144.
[24] Y. Wang, G.L. Niu, S.D. Zhai, W.J. Zhang, D. Xing, Specific photoacoustic cavitation through nucleus targeted nanoparticles for high-efficiency tumor therapy, Nano Res. 13 (3) (2020) 719–728.
[25] R. Zhang, Q. Zeng, X. Li, D. Xing, T. Zhang, Versatile gadolinium (III)-phthalocyaninate photoagent for MR/PA imaging-guided parallel photocavitation and photodynamic oxidation at single-laser irradiation, Biomaterials 275 (2021), 120993.
[26] Q.Y. Chen, J.K. Yu, K. Kim, Review: optically-triggered phase-transition droplets for photoacoustic imaging, Biomed., Eng. Lett. 8 (2) (2018) 223–229.
[27] Y. Ito, D. Veysset, S.E. Kooi, D. Martynowych, K. Nakagawa, K.A. Nelson, Interferometric and fluorescence analysis of shock wave effects on cell membrane, Commun. Phys. 3 (1) (2020) 1–6.
[28] D.A. Pereira, A.D. Silva, P.A. Martins, A.P. Piedade, D. Martynowych, D. Veysset, L. G. Arnaut, Imaging of photoacoustic-mediated permeabilization of giant unilamellar vesicles (GUVs), Sci. Rep. 11 (1) (2021) 1–12.
[29] D. Veysset, U. Gutiérrez-Hernández, L. Dresselhaus-Cooper, F. De Colle, S. Kooi, K. A. Nelson, P.A. Quinto-Su, T. Pezeril, Single-bubble and multibubble cavitation in water triggered by laser-driven focusing shock waves, Phys. Rev. E 97 (5) (2018), 053112.
[30] L.M. Liu, Q. Chen, L.W. Wen, C. Li, H. Qin, D. Xing, Photoacoustic therapy for precise eradication of glioblastoma with a tumor site blood–brain barrier permeability upregulating nanoparticle, Adv. Funct. Mater. 29 (11) (2019) 1808601.
[31] J. Zhong, L. Wen, S. Yang, L. Xiang, Q. Chen, D. Xing, Imaging-guided high-efficient photoacoustic tumor therapy with targeting gold nanorods, Nanomed. -Nanotechnol. 11 (6) (2015) 1499–1509.
[32] H. Lin, S. Gao, C. Dai, Y. Chen, J. Shi, A two-dimensional biodegradable niobium carbide (MXene) for photothermal tumor eradication in NIR-I and NIR-II biowindows, J. Am. Chem. Soc. 139 (45) (2017) 16235–16247.
[33] M. Zhao, Q. Zeng, X. Li, D. Xing, T. Zhang, Aza-BODIPY-based phototheranostic nanoagent for tissue oxygen auto-adaptive photodynamic/photothermal complementary therapy, Nano Res. 15 (1) (2022) 716–727.
[34] M. Zhou, J. Wang, J. Pan, H. Wang, L. Huang, B. Hou, H. Yu, Nanovesicles loaded with a TGF-β receptor 1 inhibitor overcome immune resistance to potentiate cancer immunotherapy, Nat. Commun. 14 (1) (2023) 3593.
[35] N.N. Wang, Z.Z. Zhao, Y.F. Lv, H.H. Fan, H.R. Bai, H.M. Meng, Y.Q. Long, T. Fu, X. B. Zhang, W.H. Tan, Gold nanorod-photosensitizer conjugate with extracellular pH-driven tumor targeting ability for photothermal/photodynamic therapy, Nano Res. 7 (9) (2014) 1291–1301.
[36] C.M. Pitsillides, E.K. Joe, X. Wei, R.R. Anderson, C.P. Lin, Selective cell targeting with light-absorbing microparticles and nanoparticles, Biophys. J. 84 (6) (2003) 4023.
[37] R.H. Groeneveld, R. Sprik, A. Lagendijk, Femtosecond spectroscopy of electron-electron and electron-phonon energy relaxation in Ag and Au, Phys. Rev. B 51 (17) (1995) 11433.
[38] Y. Shi, H. Qin, S. Yang, D. Xing, Thermally confined shell coating amplifies the photoacoustic conversion efficiency of nanoprobes, Nano Res. 9 (12) (2016) 3644.
[39] Y. Shi, S. Yang, D. Xing, New insight into photoacoustic conversion efficiency by plasmon-mediated nanocavitation: Implications for precision theranostics, Nano Res. 10 (8) (2017) 2800.
[40] B.S. Guru, H.R. Hiziroglu, Electromagnetic Field Theory Fundamentals, Cambridge university press, 2009.
[41] A. Hatef, B. Darvish, A. Dagallier, Y.R. Davletshin, W. Johnston, J.C. Kumaradas, M. Meunier, Analysis of photoacoustic response from gold–silver alloy nanoparticles irradiated by short pulsed laser in water, J. Phys. Chem. C. 119 (42) (2015) 24075.
[42] L.C. Evans, Partial differential equations, Am. Math. Soc. 19 (2010).
[43] A. Rosencwaig, A. Gersho, Theory of the photoacoustic effect with solids, J. Appl. Phys. 47 (1) (1976) 64–69.
[44] F.M. Menger, Laplace pressure inside micelles, J. Phys. Chem. 83 (1979) 893.
[45] E.P. Furlani, I.H. Karampelas, Q. Xie, Analysis of pulsed laser plasmon-assisted photothermal heating and bubble generation at the nanoscale, Lab. Chip. 12 (19) (2012) 3707.
[46] L.V. Wang, Photoacoustic Imaging and Spectroscopy, CRC press, 2017.
[47] A. Prosperetti, A generalization of the Rayleigh–Plesset equation of bubble dynamics, Phys. Fluids 25 (3) (1982) 409.
[48] A.J. Chorin, Numerical solution of the Navier-Stokes equations, Math. Comput. 22 (104) (1968) 745.
[49] American National Standard for Safe Use of Lasers; ANSI Z136.1–2007, Laser Institute of America,, Orland, FL, USA, 2007.
[50] J. Zhou, J. Zhou, W. Wang, S. Liang, L. Jing, S.H. Bo, S.L. Chen, Miniature non-contact photoacoustic probe based on fiber-optic photoacoustic remote sensing microscopy, Opt. Lett. 46 (22) (2021) 5767–5770.
[51] K.L. Bell, P.H. Reza, R.J. Zemp, Real-time functional photoacoustic remote sensing microscopy, Opt. Lett. 44 (14) (2019) 3466–3469.
[52] C.L. Chen, L.R. Kuo, S.Y. Lee, Y.K. Hwu, S.W. Chou, C.C. Chen, Y.Y. Chen, Photothermal cancer therapy via femtosecond-laser-excited FePt nanoparticles, Biomaterials 34 (4) (2013) 1128–1134.
[53] Y. Tan, X. Ding, H. Long, J. Ye, T. Huang, Y. Lin, G. Huang, Percutaneous ethanol injection enhanced the efficacy of radiofrequency ablation in the treatment of HCC: an insight into the mechanism of ethanol action, Int. J. Hyperther. 38 (1) (2021) 1394–1400.
[54] K. Koga, T. Ikeshoji, K.I. Sugawara, Size-and temperature-dependent structural transitions in gold nanoparticles, Phys. Rev. Lett. 92 (11) (2004), 115507.
[55] É. Boulais, R. Lachaine, M. Meunier, Plasma-mediated nanocavitation and photothermal effects in ultrafast laser irradiation of gold nanorods in water, J. Phys. Chem. C. 117 (18) (2013) 9386.
[56] Y.S. Chen, Y. Zhao, S.J. Yoon, S.S. Gambhir, S. Emelianov, Miniature gold nanorods for photoacoustic molecular imaging in the second near-infrared optical window, Nat. Nanotechnol. 14 (5) (2019) 465–472.

Dandan Cui is a Ph.D. candidate student from the Institute of Biophotonics of South China Normal University. Her current research focuses on photoacoustic theory and photoacoustic contrast agent to improve the contrast of lesion area imaging.

Jie Mi is a M.S. candidate student from the Institute of Biophotonics of South China Normal University. His research interests include photoacoustic spectroscopy and its applications.

Zhenhui Zhang is a Ph.D. candidate student from the Institute of Biophotonics of South China Normal University. His current research focuses on photoacoustic theory, super-resolution imaging and polarization imaging.'

Xiaoye Su is a M.S. candidate student from the Institute of Biophotonics of South China Normal University. Her research interests are in the photoacoustic molecular imaging.

Xiaodong Sun is a M.S. candidate student from the Institute of Biophotonics of South China Normal University. Her research focuses on photoacoustic theory and TEM-triggered contrast agent for dynamic contrast-enhanced photoacoustic imaging.

Gen Mu is currently pursuing his Master's degree in the Institute of Biophotonics of South China Normal University. His research interest focuses on polarization imaging.

Yujiao Shi, associate professor of the Institute of Biophotonics, South China Normal University, is committed to studying the amplification mechanism of photoacoustic conversion efficiency at the nanoscale, carrying out research on the photoacoustic conversion efficiency mechanism of nanoprobes, and theoretically exploring the quantitative photoacoustic conversion efficiency of probes under the phase transition mechanism and thermal expansion mechanism.

Sihua Yang, associate dean and professor of the Institute of Biophotonics, South China Normal University. His research fields are photoacoustic microscopy, polarized photoacoustic imaging, multimodal photoacoustic endoscopy technology and clinical applications.